Coherent Vector Based Model Predictive Control with Zero-Sequence Component Injection for Three-Level NPC Inverter Fed PMSM Drives

Xiaomei Tang, Shuangxia Niu, *Senior Member IEEE*

***Abstract*—The conventional model predictive control (MPC) selects one basic voltage vector through the enumeration process, which will result in relatively high steady-state fluctuation and random switching actions, especially when the motor operates in low-speed areas. To enhance the control performance, a three-level neutral-point-clamped (NPC) inverter is applied, although this increases the complexity of the control algorithm for permanent magnet synchronous motor (PMSM). In the proposed MPC scheme, a set of coherent voltage vectors (CVVs) with movable starting points is introduced to replace the basic candidates. The pulse train of the optimal CVV is generated by single-carrier modulation, and capacitor charge balancing in different sectors can be included in the zero-sequence component injection. The proposed CVV-MPC is characterized by simple implementation and satisfactory performance under low switching frequency. Comparative experiments are conducted to verify the effectiveness and superiority of the proposed method.**

***Index Terms*—Model predictive control (MPC), permanent magnet synchronous motor (PMSM), three-level neutral-point-clamped (3L-NPC) inverter.**

I. Introduction

In the past decades, the three-level neutral-point clamped (3L-NPC) inverter has been widely utilized in various industrial applications, such as electrical railway traction and motor drives [1]. Compared with the conventional three-phase two-level inverter, 3L-NPC inverters own many salient advantages, including lower output harmonics, alleviated power device voltage stress, reduced dV/dt, etc [2]–[4]. This makes it ideally suited as a bridge between permanent magnet synchronous motors (PMSMs) and DC sources, providing high-performance driving effects. Thus, the PMSM drives fed by a 3L-NPC inverter are studied in this paper.

In recent years, various control techniques have been extensively investigated, which is vital to electric drive systems [5]. Field-oriented control (FOC) with a proportional integral (PI) and direct torque control (DTC) are the two commonly employed approaches. As a linear controller, PI can yield a stable drive performance by setting the appropriate gain parameters [6]. However, bandwidth issues limit the improvements in its dynamic performance. DTC considers the inverter and the motor as a whole system, and it directly selects one appropriate voltage vector without pulsewidth modulator [7]. Although DTC has a fast dynamic response and strong robustness, the torque ripples inevitably increase.

Different from these classical approaches based on feedback concepts, finite-control-set model predictive control (FCS-MPC) has attracted wide attention [8]. FCS-MPC features a straightforward control structure, quick dynamic response, and easy implementation of multiple constraints [9]. The conventional FCS-MPC predicts the future states of the PMSM and evaluates all feasible output voltage of an inverter. For the 3L-NPC drive system, the predictive model and cost function need to be called 27 times respectively. However, it will produce significant steady-state ripples due to low average switching frequency since it only applies one optimal voltage vector in each control period [10].

Increasing the sampling rate is the most direct way to refine the performance of MPC during steady state, but this makes its digital implementation difficult [11], [12]. To address these issues, the prediction horizon is extended to 5 steps, which performs better than the single-step MPC under a low sampling frequency in [13]. Based on the concept of virtual voltage vectors (VVVs), Liu *et al.* expand the control sets to different amplitudes and angles [14]. In [15], 48 VVVs are constructed by means of discrete space vector modulation.

MPC is also often implemented for grid-tied power converters. In [16], virtual space vector-based MPC is applied to a microgrid connected to the main grid, which includes an energy storage system and solar power generation. The method significantly improves the neutral point voltage balance and output quality. To achieve robust characteristics against grid impedance variations, an improved discrete space vector modulation is proposed [17]. Without the need for any lookup table initialization process, the search range can be narrowed down by simply determining a single sector and two concentric hexagonal diagrams. In [18], a cascaded structure is used to optimally achieve the two control targets of predictive current and capacitor voltage in a phased manner.

Many other advanced techniques have been put forward, such as MPC with multivectors and duty-cycle optimization-based MPC. In [19], an active voltage vector along with a zero voltage vector is applied over the whole control period, and their optimal timing calculation is based on the q-axis current slopes. In [20], an equivalent three-vector-based MPC is proposed, and the conventional voltage vector space is

This work was supported in part by the the Research Grant Council of the Hong Kong Government under Projects PolyU 152109/20E and in part by RGC Collaborative Research Fund under Grant C1052-21G. (Corresponding author: Shuangxia Niu)

Xiaomei Tang, Shuangxia Niu are with the Department of Electrical and Electronic Engineering, The Hong Kong Polytechnic University, Hong Kong 999077, China (e-mail: 21040654r@connect.polyu.hk; shuangxia.niu@polyu.edu.hk.)

reconstructed. In [21], the output voltage levels are modified by adjusting the duty cycle. The optimal duty-cycle corrections are determined based on current tracking error, which helps reduce current distortion. To optimize the duty cycle for each of the 24 redivided sectors, Donoso *et al.* made use of the numerical values of cost functions [22]. The similarity between these different variants of MPC is that they are required to determine not only the optimal combination of output variables but also every variable's action time, which is computationally intensive.

Therefore, several strategies have been investigated to handle this key issue in recent years. Some schemes are devoted to the deadbeat control for a fast transient response. Based on the principle of deadbeat, Xie *et al.* adopt the predictive voltage calculation instead of the current prediction [23]. Meanwhile, the number of cost function calculations is reduced. However, the scheme cannot solve the control constraints. In [24], the sector label of the reference voltage is first d etermined by the deadbeat principle, and then two non-zero vectors and one zero vector are selected. However, a remarkable steady-state error will occur due to the simple current control without compensation. Another common approach is eliminating the enumeration process and simplifying the selection of voltage vectors. In [25], for example, the optimal vector combination is determined according to the stator flux p osition a nd the torque deviation. A low-complexity algorithm is proposed for three-level inverter in [21], which reduces the candidate cases to only seven.

Another inherent issue for MPC of the 3L-NPC inverter is the neutral-point voltage unbalance, which will affect the reliability and lifetime of the PMSM drive system. Generally, balancing the neutral-point voltage can be achieved by adding objective terms to the predefined c ost f unction, w hich also takes full advantage of the multi-objective nature of MPC strategies [26], [27]. However, different control targets are required to be equipped with proper weighting factors, the performance of each objective is coupled with each other. The weighting factors are required to be fine-tuned b y trial and error, which consumes a lot of time and sacrifices the fast dynamic response. Yang *et al.* balanced the neutral-point voltage by selecting proper redundant small voltage vectors [28]. The candidate voltage vectors to be evaluated are effectively reduced, and the weighting factors are eliminated as well. Zhou *et al.* decoupled the control process into two stages in each control period and considered the nonlinearity of the voltage vectors caused by the unbalanced neutral-point voltage [29]. A novel balanced zero-sequence voltage injection method to maximize fault tolerance was proposed by Li *et al* [30]. It not only simplifies the calculation, but also achieves the combination with neutral offset.

Although these recently emerged studies have been able to enhance steady-state performance while balance neutral-point voltage, the computational cost will further increase. For example, if double vectors are applied in the entire control cycle, there are totally 729 (27^2) possible combinations to be enumerated and evaluated [31]. When the consideration of neutral voltage balance is included, the complexity of this assumed double-vector strategy will increase exponentially. Complex formulation to solve the optimization problem will deteriorate the system's dynamic performance and hinder its practical application [32]. Thus, it is vital to find a novel MPC algorithm that can simultaneously achieve smooth, error-free output and reduce the complexity of online optimization.

This article investigates a coherent voltage vector-based model predictive control (CVV-MPC) of 3L-NPC inverters. Unlike the improved MPC mentioned above, the 27 basic voltage vectors of a three-level inverter are coherentized before being applied to predict the following instant operating states. Only the finite set of coherent voltage vectors adjacent to the previous output voltage is formulated, which is computationally efficient. The abrupt change in the output voltage can be simply and effectively avoided, thus realizing a smooth and accurate control effect. The balance of neutral-point voltage is explicitly considered in the prediction process to synthesize the optimal coherent voltage vector. Different from [26], the proposed method does not employ the PWM generator to produce desired gate drive signals. In order to reduce current distortion with a relatively lower sampling rate, a single carrier mode applicable to the above algorithms is implemented, not limited to original modulation schemes such as symmetrical seven-segment.

The rest of this paper is organized as follows. Section II introduces the basic topology of 3L-NPC PMSM inverter drives and the principles of conventional FCS-MPC. Section III presents the proposed CVV-MPC method, including delay compensation, calculation of coherent voltage vectors, neutral-point capacitor voltage balance, and generation of switching signals. The experimental studies and comparative analysis of different MPC methods are given in Section IV. In Section V, the conclusions are drawn.

II. Model of 3L-NPC PMSM Drives and FCS-MPC Methods

A. Topology and Switching States of 3L-NPC Inverter

Fig.1 shows the topology of the 3L-NPC inverter, V_{dc} is constant DC bus voltage, U_{C_1} and U_{C_2} are DC-link bus top and bottom capacitor voltages respectively. Assuming that the two capacitors (C_1 and C_2) are perfectly charged to an equal value of $V_{dc}/2$.

Variables $U_x(x = a, b, c)$ respectively express the node voltage of three-phase arms. Taking Phase A as an example, the four IGBTs, (S_{a1},S_{a3}) and (S_{a2},S_{a4}), are complementary switching pairs, with only half the voltage stress on each IGBT compared to the two-level inverter. Each phase arm, therefore, has three switching states, the corresponding output value of U_a (U_b or U_c) may be $-\frac{V_{dc}}{2}$, 0 or $\frac{V_{dc}}{2}$. For convenience, $-\frac{V_{dc}}{2}$, 0 and $\frac{V_{dc}}{2}$ are labeled as N, O and P. Fig 2 shows the total space voltage vectors diagram generated from 27 switching states. The voltage vector in the stationary $\alpha\beta$ coordinate system is given by:

$$\begin{aligned} \boldsymbol{u}_s &= \frac{2}{3}\left(U_a + U_b\boldsymbol{a} + U_c\boldsymbol{a}^2\right) \\ &= \frac{V_{\mathrm{dc}}}{3}\left(S_a + S_b\boldsymbol{a} + S_c\boldsymbol{a}^2\right) \end{aligned} \tag{1}$$

where $\boldsymbol{u}_s = u_{s\alpha} + ju_{s\beta}$ refers to voltage vector supplied to machine terminals, $S_x \in \{1, 0, -1\}$ corresponds to three different

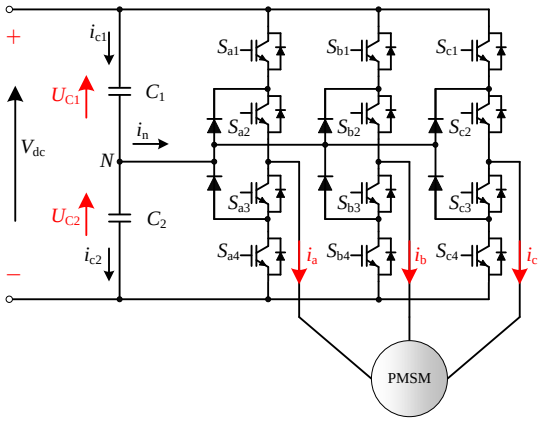

Fig. 1. Topology of three-level NPC inverter.

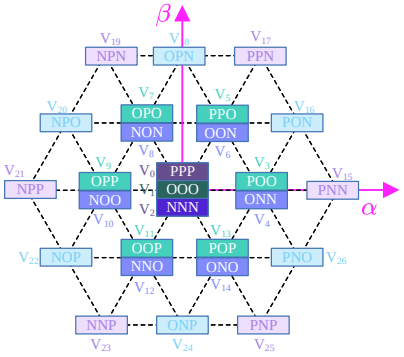

Fig. 2. Space voltage vectors diagram and 27 output states for the three-level inverter.

voltage levels. $\boldsymbol{a} = e^{j2\pi/3}$ represents phase displacement of $2\pi/3$ among three phases.

B. Mathematical Model of PMSM

This paper focuses on surface-mounted PMSM, which have the same dq-axis stator inductances, i.e., $L_d = L_q = L$. The machine model in the stationary $\alpha\beta$-axis can be expressed as follows:

$$L\frac{d\boldsymbol{i_s}}{dt} = \boldsymbol{u}_s - R_s\boldsymbol{i}_s - \underbrace{j\omega_e\psi_f e^{j\theta_r}}_{\boldsymbol{u}_e} \tag{2}$$

where $\boldsymbol{i}_s$ is the stator current; R_s is the nominal stator resistance. ψ_f is the flux linkage generated by the permanent magnet on the rotor side; ω_e is the rotor electrical speed. $\boldsymbol{u}_e = j\omega_e\psi_f e^{j\theta_r}$ denotes the back electromagnetic force, and θ_r is the electrical rotor position.

And the mechanical equations for a surface-mounted PMSM can be expressed as the cross product of the stator flux and current as

$$T_e = p_n\boldsymbol{\psi}_s \times \boldsymbol{i_s} \tag{3}$$

where p_n represents the number of pole pairs of the motor.

And the mechanical rotor speed is calculated using the following equation

$$\dot{\omega}_m = -\frac{D}{J}\omega_m + \frac{1}{J}\left(T_e - T_l\right) \tag{4}$$

where J is the rotor inertia, T_l is the load torque, D is the viscous friction coefficient, and $\omega_m = \omega_e/p_n$ is the mechanical rotor speed.

C. Predictive Models and FCS-MPC Strategy

For small sampling time, the forward Euler algorithm is applied to (2). And discrete-time predictive currents can be obtained, as shown in (5).

$$\boldsymbol{i}_s(k+1) = \boldsymbol{i}_s(k) + \frac{T_s}{L}\left(\boldsymbol{u}_s(k) - R_s\boldsymbol{i}_s(k) - \boldsymbol{u}_e(k)\right) \tag{5}$$

where T_s is the sampling time, k is the sampling interval. $\boldsymbol{i}_s(k)$ and $\boldsymbol{u}_s(k)$ are stator current and voltage in k-th instant, respectively. $\boldsymbol{i}_s(k+1)$ is the prediction in $(k+1)$-th instant.

Then, (2) is transformed to the rotor reference frame and rearranged as

$$\begin{aligned} i_{\mathrm{qs}}(k+1) = i_{\mathrm{qs}}(k) + \frac{T_s}{L}[&-R_s i_{\mathrm{qs}}(k) + \omega_e(k)Li_{\mathrm{ds}}(k) \\ &+u_{\mathrm{qs}}(k) - \psi_f\omega_e(k)] \end{aligned} \tag{6}$$

$$\begin{aligned} i_{\mathrm{ds}}(k+1) =& i_{\mathrm{ds}}(k) \\ &+ \frac{T_s}{L}\left[-R_s i_{\mathrm{ds}}(k) + \omega_e(k)Li_{\mathrm{qs}}(k) + u_{\mathrm{ds}}(k)\right] \end{aligned} \tag{7}$$

where i_{ds} and i_{qs} are the direct and quadrature components of the stator current, the same applies to the stator voltage.

The neutral-point voltage drift is defined as the difference between upper capacitor and lower capacitor voltage:

$$U_{\mathrm{npv}} = U_{C_1} - U_{C_2} \tag{8}$$

Discrete-time predictive U_{npv} can be represented as

$$U_{\mathrm{npv}}(k+1) = U_{npv}(k) + \frac{T_s}{C}\left(Q_a i_a(k) + Q_b i_b(k) + Q_c i_c(k)\right) \tag{9}$$

where $C = C_1 = C_2$ is the capacitor value and Q_x (x = a, b, c) depends on the voltage level of each phase and is defined as

$$Q_x = \begin{cases} 1 & \text{if } S_x = 0 \\ 0 & \text{otherwise} \end{cases} \tag{10}$$

The conventional FCS-MPC takes all 27 vectors into (5) to calculate predictive currents at the next sampling time and then uses the predictive currents to calculate cost function as follows:

$$J = \left[i_{ds}^* - i_{ds}(k+1)\right]^2 + \left[i_{qs}^* - i_{qs}(k+1)\right]^2 \tag{11}$$

where i_{ds}^* is the d-axis reference current. To maximize the motor torque, set $i_{ds}^* = 0$. In this way, $\boldsymbol{i}_s$ is at 90° to the rotor flux vector. i_{qs}^* is the q-axis reference current, which is generated from the PI controller of the outer speed loop.

The vector that can minimize the cost function is selected and used in the next sampling time. The control process of the conventional FCS-MPC control method with a 3L-NPC inverter consists of the outer speed loop and the inner stator current loop. Conventional FCS-MPC only has a single control objective, which is to minimize the current tracking error, and the neutral-point voltage balance does not take into account. Applying only one basic vector per sampling cycle results in

very unsmooth output. Meanwhile, a total of 27 switching states are in the alternative list, and each basic vector needs to be predicted by (5) and calculated by (11), which causes a heavy computational burden on the processor and makes it difficult to operate at high switching frequency. The total calculation time per sampling period is up to 54, and 8 redundant voltage vectors are also accounted for.

III. Principle of The Proposed CVV-MPC

A. Delay Compensation

To compensate for one-step delay, it is essential to predict forward two steps at kth with $\boldsymbol{i}_s(k)$ as the initial condition and obtain the predicted value $\boldsymbol{i}_s(k+2)$. First, the stator current and rotor position at kth instant are sensed, and the applied voltage vector $\boldsymbol{u}_s(k)$ is considerated. Then substitute them into (6) and (7) to predict $i_{ds}(k+1)$ and $i_{qs}(k+1)$. Finally, predict the impact of different candidate voltage vectors on current during the $(k+2)$th control cycle:

$$\begin{aligned} i_{qs}(k+2) = i_{qs}(k+1) + \frac{T_s}{L}[-R_s i_{qs}(k+1) - \omega_e(k+1) \\ Li_{ds}(k+1) + u_{qn} - \psi_f \omega_e(k+1)] \end{aligned} \tag{12}$$

$$\begin{aligned} i_{ds}(k+2) = i_{ds}(k+1) + \frac{T_s}{L} \\ [-R_s i_{ds}(k+1) + \omega_e(k+1) L i_{qs}(k+1) + u_{dn}] \end{aligned} \tag{13}$$

where the integer n=0, 1, 2 ...26 corresponds to the vector numbers shown in Fig. 2. In this way the optimal voltage vector for $(k+1)$th instant is calculated at kth instant and will be applied to the inverter at $(k+1)$th, thus the one-step delay in voltage and current is compensated.

B. Voltage Vector Coherence

In the FCS-MPC presented in the previous section, the best voltage vector is selected among the 27 available vectors and applied during the entire control period. This will cause the output voltage to change abruptly, and is also computationally inefficient. To address these maladies, we introduce the concept of coherent voltage vector, which relates the voltage vectors of the current time step to the previous step. The candidate set is modified as follows:

$$\boldsymbol{u}_{dqn}^{c}(k) = \varepsilon_\alpha \boldsymbol{u}_{dq}^{c}(k-1) + (1-\varepsilon_\alpha)\, \boldsymbol{u}_{dqn} \tag{14}$$

where $\boldsymbol{u}_{dqn}$ denote different candidate voltage vectors, ε_α denotes the degree of coherence and takes values in the interval [0, 1), the larger ε_α is, the more pronounced the coherence of the voltage is.

In order to avoid repeated calculation of redundant vectors and reduce the number of calls to the formula, the original voltage vector shown in Fig. 2 is simplified, a nd o nly the outermost 6 vectors are considered. Such u_{dqn} intervals of 60° also make full use of the rich vector resources of the three-level inverter. Fig. 3 shows the candidate vector selection for several control cycles, which have been coherentized. Therefore, the cost function considering the delay compensation is constructed as:

$$J = \left|i_d^* - i_d^c(k+2)\right|^2 + \left|i_q^* - i_q^c(k+2)\right|^2 \tag{15}$$

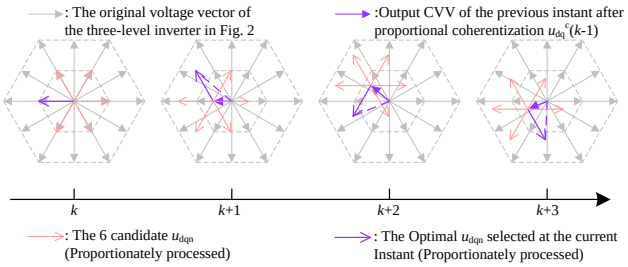

Fig. 3. Optimal CVV selection process in several control cycles.

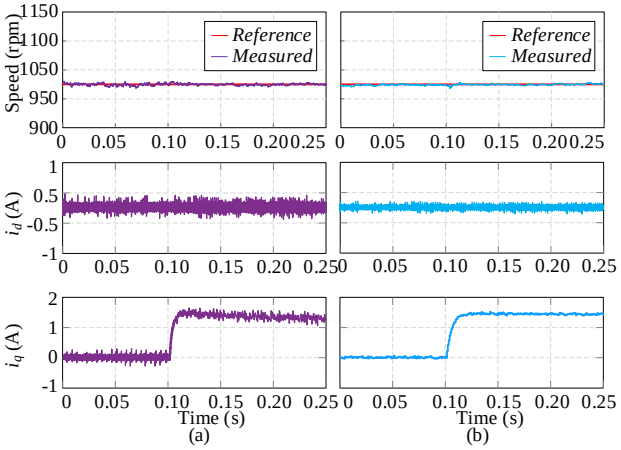

Fig. 4. Performance comparison of a 2 Nm load torque applied at 0.1s. (a) ε_α=0.3. (b) ε_α=0.5.

From analysis (14), we can know that if ε_α is too large, it will reduce the output capability and affect the tracking of the reference value. When ε_α is zero, it is exactly the same as before the coherentization process. Therefore, it is necessary to set an upper limit for ε_α to ensure that the dynamic response can be at the same level as conventional control methods. Fig. 3 illustrates the scenario when ε_α=0.5, a value chosen to ensure that the cut-off frequency is approximately equal to the bandwidth of the conventional MPC, while also maintaining the coherence of the CVVs. Fig. 4 presents the simulation results with ε_α set to 0.3 and 0.5, respectively, demonstrating that there is little difference in current tracking performance during sudden torque changes. It is evident that 0.5 serves as the optimal value for coherence while ensuring adequate dynamic performance.

C. Optimal CVV Synthesis with Neutral-Point Capacitor Voltage Balance

Among the 6 u_{dqn}^c pointing in different directions, the one with the smallest cost function is selected as the optimal CVV. After that, its corresponding active vectors group and duration time need to be determined in the conventional methods. In this paper, a novel vector space decomposition adapted to the concept of vector coherence is employed to reduce the computational complexity without the need for multiple optimizations. Therefore, we must first know the precise sector of u_{dq}^c according to the geometric relationship. The desired

TABLE I
CVV SECTOR JUDGMENT

Sector number (N)	Corresponding CVV	S_a	S_b	S_c
I	u_1^c	$\geqslant 0$	$\leqslant 0$	$\leqslant 0$
II	u_2^c	$\geqslant 0$	$\geqslant 0$	$\leqslant 0$
III	u_3^c	$\leqslant 0$	$\geqslant 0$	$\leqslant 0$
IV	u_4^c	$\leqslant 0$	$\geqslant 0$	$\geqslant 0$
V	u_5^c	$\leqslant 0$	$\leqslant 0$	$\geqslant 0$
VI	u_6^c	$\geqslant 0$	$\leqslant 0$	$\geqslant 0$

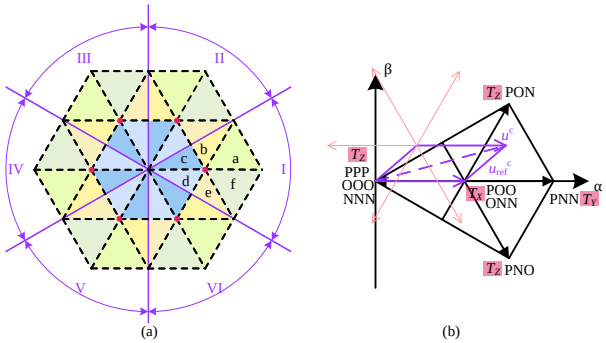

Fig. 5. Quadrilateral sectors and CVV synthesis. (a) Division of I-VI sectors.(b) CVV synthesis path in sector I and corresponding vectors.

CVV in the stationary $\alpha - \beta$ reference frame is obtained through inverse Park transformation:

$$\begin{bmatrix} u_\alpha^c \\ u_\beta^c \end{bmatrix} = \begin{bmatrix} \cos\theta & -\sin\theta \\ \sin\theta & \cos\theta \end{bmatrix} \begin{bmatrix} u_d^c \\ u_q^c \end{bmatrix}. \tag{16}$$

Transform it to the per unit format taking V_{dc} as benchmark and represent it as the three-phase symmetric form:

$$\begin{cases} u_a^* = m \cdot \sin\theta \\ u_b^* = m \cdot \sin\left(\theta - \frac{2\pi}{3}\right) \\ u_c^* = m \cdot \sin\left(\theta + \frac{2\pi}{3}\right) \end{cases} \tag{17}$$

where $m = \sqrt{3} \cdot V^c / V_{\mathrm{dc}}$, $\theta = \omega t$ (ω is the angular frequency).

In existing studies, the three-level vector space is often divided into six sub-hexagons [33], [34], which are simplified to two-level algorithms to narrow the range of optimization search and reduce switching losses. However, adjacent sub-hexagons have overlapping areas. As shown in Fig. 5(a), this paper designs a more reasonable sector division method by combining the properties of the sub-hexagon rule. The sector position can be determined directly based on the number of u_n^c that minimizes the cost function. As shown in Fig. 5(b), each u_n^c can also be regarded as synthesized from the center vector of each quadrilateral sector as the starting point. This eliminates the need to call the inverse trigonometric function and the cumbersome sector judgment and sub-sector judgment processes. The relationship between u_n^c and sector number N is shown in Table I.

In this subsection, an efficient zero-sequence component injection algorithm is implemented, which make full use of the sign law of S_x in Table I. The conventional approach requires iterative determination of the positive and negative phase voltages after superimposing the zero-sequence components,

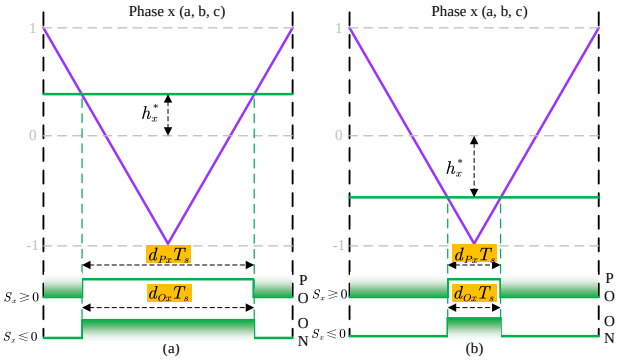

Fig. 6. Single carrier modulation mode. (a) Generation of duty cycle when h_{x}^* is positive. (b) Generation of duty cycle when h_{x}^* is negative.

and eliminating this process can save a lot of computational resources. The corrected modulation wave h_{x}^* of each phase is:

$$h_{\mathrm{x}}^* = \frac{2}{\sqrt{3}} u_{\mathrm{x}}^* + u_{\mathrm{zs}} \tag{18}$$

Since each sector corresponds to a specific combination of switching function signs, the required CVV can be achieved only by changing the duty cycle of single carrier. Fig. 6 shows the adopted single carrier modulation mode, which greatly reduces the amount of computation and simplifies the modulation process while providing strong neutral-point voltage balancing. By comparing the green modulated wave with the purple carrier wave, switching signals that contains two states $S_x \in \{1, 0\}$ or $S_x \in \{0, -1\}$ are produced. According to (9), only when the output state of a phase is O, the load current of that phase flows through the neutral-point and has an effect on the neutral-point potential. The relationship between the average neutral-point current and the load current as well as the three-phase switching state in one control cycle is as follows:

$$\bar{i}_{\mathrm{NP}} = d_{\mathrm{Oa}} i_{\mathrm{a}} + d_{\mathrm{Ob}} i_{\mathrm{b}} + d_{\mathrm{Oc}} i_{\mathrm{c}} \tag{19}$$

where d_{Ox} denotes the O-state duty cycle of phase x, which is calculated with respect to the positive or negative of S_x:

$$d_{\mathrm{Ox}} = 1 - |d_{\mathrm{NPx}}| = \begin{cases} (1 - h_{\mathrm{x}}^*)/2, & S_{\mathrm{x}} > 0 \\ (1 + h_{\mathrm{x}}^*)/2, & S_{\mathrm{x}} \leq 0 \end{cases} \tag{20}$$

Taking CVV located in sector I as an example, substituting (18) and (20) into (19):

$$
\begin{aligned}
\bar{i}_{\mathrm{NP}} &= \frac{1-h_{\mathrm{a}}^*}{2} i_{\mathrm{a}} + \frac{1+h_{\mathrm{b}}^*}{2} i_{\mathrm{b}} + \frac{1+h_{\mathrm{c}}^*}{2} i_{\mathrm{c}} \\
&= \frac{1}{2}\left[h_{\mathrm{a}}^*\left(i_{\mathrm{b}}+i_{\mathrm{c}}\right) + h_{\mathrm{b}}^* i_{\mathrm{b}} + h_{\mathrm{c}}^* i_{\mathrm{c}}\right] \\
&= \frac{1}{2}\left[\left(h_{\mathrm{a}}^*+h_{\mathrm{b}}^*\right) i_{\mathrm{b}} + \left(h_{\mathrm{a}}^*+h_{\mathrm{c}}^*\right) i_{\mathrm{c}}\right] \\
&= \frac{1}{2}\left[\left(\frac{2u_{\mathrm{a}}^*}{\sqrt{3}} + \frac{2u_{\mathrm{b}}^*}{\sqrt{3}} + 2u_{\mathrm{zs}}\right) i_{\mathrm{b}} + \left(\frac{2u_{\mathrm{a}}^*}{\sqrt{3}} + \frac{2u_{\mathrm{c}}^*}{\sqrt{3}} + 2u_{\mathrm{zs}}\right) i_{\mathrm{c}}\right] \\
&= \frac{1}{2}\left[\left(-\frac{2u_{\mathrm{c}}^*}{\sqrt{3}} + 2u_{\mathrm{zs}}\right) i_{\mathrm{b}} + \left(-\frac{2u_{\mathrm{b}}^*}{\sqrt{3}} + 2u_{\mathrm{zs}}\right) i_{\mathrm{c}}\right] \\
&= -\left[u_{\mathrm{zs}} i_{\mathrm{a}} + \frac{1}{\sqrt{3}}\left(u_{\mathrm{b}}^* i_{\mathrm{c}} + u_{\mathrm{c}}^* i_{\mathrm{b}}\right)\right]
\end{aligned}
\tag{21}
$$

To achieve active control of the neutral-point potential balance, the DC bus capacitor voltage variation is detected and feedback correction is formed. The relationship between the voltage deviation U_{npv} and the neutral-point current within a control cycle is:

$$
U_{\mathrm{npv}} = U_{\mathrm{C_1}} - U_{\mathrm{C_2}} = \bar{i}'_{\mathrm{NP}} T_{\mathrm{s}} / C \tag{22}
$$

where $\bar{i}'_{\mathrm{NP}}$ is the average increment of the neutral-point current caused by the charging and discharging of the capacitors, which requires adjusting the zero-sequence voltage injection amount.

$$
\bar{i}_{\mathrm{NP}} + \bar{i}'_{\mathrm{NP}} = 0 \tag{23}
$$

$$
u_{\mathrm{zs}} = \frac{1}{i_{\mathrm{a}}}\left[\frac{C U_{\mathrm{npv}}}{T_{\mathrm{s}}} - \frac{1}{\sqrt{3}}\left(u_{\mathrm{b}}^* i_{\mathrm{c}} + u_{\mathrm{c}}^* i_{\mathrm{b}}\right)\right] \tag{24}
$$

In the same way, the expressions of the zero-sequence components in the six sectors can be found in Table II.

An exact mathematical relationship between the neutral-point average current and the zero-sequence component is established in each small quadrilateral sector of the simplified t hree-level v ector s pace. I t c an b e s een t hat o nly the original CVV, the output current, and the upper and lower capacitor voltages are needed to generate the zero-sequence components required to balance the neutral-point potential, and the expression is simple and does not contain complex trigonometric calculations. Its computational complexity is significantly reduced as well. After simulation verification, the computation time for its prediction optimization is only about 10% of that required by the strategy in [22]. With vector coherence, only 6 evaluations are needed to determine the optimal solution, eliminating the necessity for precise sector localization.

D. Pulse Train Generation

Once we have found the optimal CVV through the cost function and synthesize it with single carrier zero-sequence injection method, we next need to generate switching signals based on it. To prevent duty cycle saturation, resulting in output voltage distortion, the zero-sequence component must be reasonably limited.

$$
\begin{cases}
u_{\mathrm{zsmax}} = 1 - \frac{2}{\sqrt{3}} \max\left(u_a^*, u_b^*, u_c^*\right) \\
u_{\mathrm{zsmin}} = -1 - \frac{2}{\sqrt{3}} \min\left(u_a^*, u_b^*, u_c^*\right)
\end{cases} \tag{25}
$$

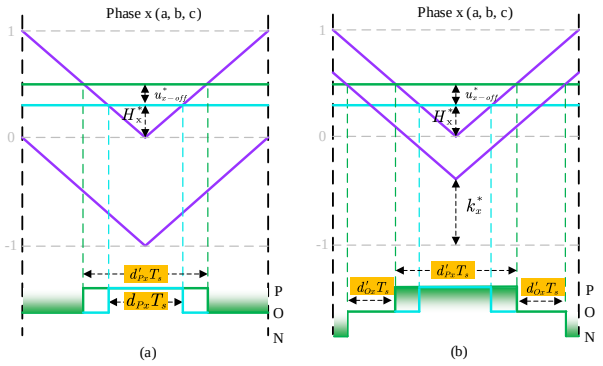

Fig. 7. Dual-carrier modulation mode under initial and improved modulated waves. (a) Two carriers are fixed. (b) Lower carrier is adjustable.

When the injected zero-sequence component goes up to u_{zsmax} or down to u_{zsmin}, the duty cycle of one phase will becomes 1, and the switch does not operate during this cycle. Under these conditions, in order to maintain the regulating capability of the neutral-point balance, a dual-carrier modulation is taken to generate the desired switching signals. As shown in Fig. 7, the charge is balanced in one control cycle under the effect of the compensation amount, and it can be derived as:

$$
u_{\mathrm{off}}^* = \frac{C\left(U_{C_1} - U_{C_2}\right) + \sum_{\mathrm{x=a,\ b,c}} d_{\mathrm{Ox}} i_{\mathrm{x}}}{\sum_{\mathrm{x=a,\ b,c}} \mathrm{sign}\left(h_{\mathrm{x}}^*\right) i_{\mathrm{x}}}. \tag{26}
$$

E. Control Block Diagram and Implementation Steps

Based on the above analysis, the proposed control strategy is implemented in three progressive stages shown in Fig. 8. In summary, the proposed strategy can be implemented in the following steps:

Step 1 Measurement: Sample the motor speed and rotor position, as well as the stator currents $\boldsymbol{i}_s$. Record the voltage vector applied at the current moment.

Step 2 Desired value calculation: Develope the discrete mathematical model of PMSM. Like the conventional FCS-MPC method, use the external speed loop to obtain the current reference i_q^* and set i_d^* to 0.

Step 3 CVV selection: The original voltages pointing in different directions are coherent through (14) and synthesized into u_{dq}^n together with the state of the output of the previous moment. Predict the future states of the current at $(k+2)$th instant for all candidate CVVs by the discrete models in (12) and (13). This operation is designed to offset delays due to the computational process and ensure the timeliness of the control response. The cost function J is evaluated, and the u_{dq}^n correspongding to the minimal current error is selected.

Step 4 Zero-sequence component injection: Use the voltage deviation U_{npv} on the DC bus side to calculate the average neutral-point current $\bar{i}_{\mathrm{NP}}$. According to Table II, based on the quadrilateral sector number where the optimal CVV is located, the corresponding zero-sequence component u_{zs} used to balance the neutral-point potential is calculated. The modified modulated wave amplitude h_{x}^* is then obtained from (18).

TABLE II
NEUTRAL-POINT CURRENTS AND ZERO SEQUENCE VOLTAGES IN SIX SECTORS

Sector	$\bar{i}_{\mathrm{NP}}$	u_{zs}
I	$-\left[u_{\mathrm{zs}}i_{\mathrm{a}}+\frac{1}{\sqrt{3}}\left(u_{\mathrm{b}}^{*}i_{\mathrm{c}}+u_{\mathrm{c}}^{*}i_{\mathrm{b}}\right)\right]$	$\frac{1}{i_{\mathrm{a}}}\left[\frac{CU_{\mathrm{npv}}}{T_{\mathrm{s}}}-\frac{1}{\sqrt{3}}\left(u_{\mathrm{b}}^{*}i_{\mathrm{c}}+u_{\mathrm{c}}^{*}i_{\mathrm{b}}\right)\right]$
II	$u_{\mathrm{zs}}i_{\mathrm{c}}+\frac{1}{\sqrt{3}}\left(u_{\mathrm{a}}^{*}i_{\mathrm{b}}+u_{\mathrm{b}}^{*}i_{\mathrm{a}}\right)$	$\frac{1}{i_{\mathrm{a}}}\left[\frac{CU_{\mathrm{npv}}}{T_{\mathrm{s}}}-\frac{1}{\sqrt{3}}\left(u_{\mathrm{b}}^{*}i_{\mathrm{c}}+u_{\mathrm{c}}^{*}i_{\mathrm{b}}\right)\right]$
III	$-\left[u_{\mathrm{zs}}i_{\mathrm{b}}+\frac{1}{\sqrt{3}}\left(u_{\mathrm{a}}^{*}i_{\mathrm{c}}+u_{\mathrm{c}}^{*}i_{\mathrm{a}}\right)\right]$	$\frac{1}{i_{\mathrm{a}}}\left[\frac{CU_{\mathrm{npv}}}{T_{\mathrm{s}}}-\frac{1}{\sqrt{3}}\left(u_{\mathrm{b}}^{*}i_{\mathrm{c}}+u_{\mathrm{c}}^{*}i_{\mathrm{b}}\right)\right]$
IV	$u_{\mathrm{zs}}i_{\mathrm{a}}+\frac{1}{\sqrt{3}}\left(u_{\mathrm{b}}^{*}i_{\mathrm{c}}+u_{\mathrm{c}}^{*}i_{\mathrm{b}}\right)$	$\frac{1}{i_{\mathrm{a}}}\left[\frac{CU_{\mathrm{npv}}}{T_{\mathrm{s}}}-\frac{1}{\sqrt{3}}\left(u_{\mathrm{b}}^{*}i_{\mathrm{c}}+u_{\mathrm{c}}^{*}i_{\mathrm{b}}\right)\right]$
V	$-\left[u_{\mathrm{zs}}i_{\mathrm{c}}+\frac{1}{\sqrt{3}}\left(u_{\mathrm{a}}^{*}i_{\mathrm{b}}+u_{\mathrm{b}}^{*}i_{\mathrm{a}}\right)\right]$	$\frac{1}{i_{\mathrm{a}}}\left[\frac{CU_{\mathrm{npv}}}{T_{\mathrm{s}}}-\frac{1}{\sqrt{3}}\left(u_{\mathrm{b}}^{*}i_{\mathrm{c}}+u_{\mathrm{c}}^{*}i_{\mathrm{b}}\right)\right]$
VI	$u_{\mathrm{zs}}i_{\mathrm{b}}+\frac{1}{\sqrt{3}}\left(u_{\mathrm{a}}^{*}i_{\mathrm{c}}+u_{\mathrm{c}}^{*}i_{\mathrm{a}}\right)$	$\frac{1}{i_{\mathrm{a}}}\left[\frac{CU_{\mathrm{npv}}}{T_{\mathrm{s}}}-\frac{1}{\sqrt{3}}\left(u_{\mathrm{b}}^{*}i_{\mathrm{c}}+u_{\mathrm{c}}^{*}i_{\mathrm{b}}\right)\right]$

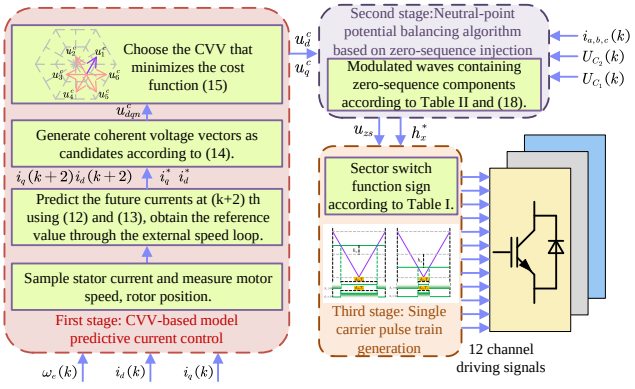

Fig. 8. Block diagram of proposed MPC algorithm.

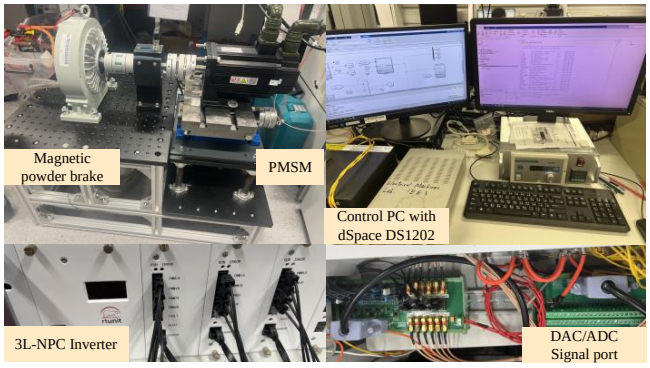

Fig. 9. Test bench of the 3L-NPC inverter system.

Step 5 Switching pulses generation: Before the final reference voltage h_{x}^{*} is output, it is limited according to (25). Based on the switching function signs in Table II, h_{x}^{*} is converted to a two-channel signals, and then, with only a single triangular carrier to compare with, four drive signals can be generated.

IV. EXPERIMENTAL RESULTS

In order to investigate the performance of the proposed method, a series of experiments have been carried out with a 3L-NPC-fed PMSM drive. The test rig is depicted in Fig. 9. A dSPACE MicroLabBox DS1202 is used as the controller, and the 3L-NPC inverter is composed of IGBT. Table III lists the detailed parameters of the PMSM and inverter. Current probes (Keysight N2783B) are adopted to measure the three-phase motor currents, and the experimental waveform is displayed in a digital oscilloscope (Tektronix MDO3024). The test bench integrates torque and speed sensors and a magnetic powder brake, which can provide speed and torque information.

A. Steady-State Performance Comparison

First, the steady-state performance tests were carried out under the command of 500 r/min with rated load. To verify the superiority of the proposed method, the experimental results of the conventional multi-virtual-vector MPC (M2V-MPC) [35] with the same sampling and switching frequency were also presented. The waveforms of speed, three-phase currents for the two methods are shown in Fig. 10, as well as the phase a current harmonic spectrum and the scaled-up d-axis current.

TABLE III
PARAMETERS OF THE PMSM DRIVE SYSTEM

Parameter	Description	Value
V_{dc}	DC-link voltage	240 V
L	dq-axes inductance	1.55 mH
R_s	Stator resistance	0.65 Ω
ψ_f	Rotor flux linkage	0.225 Wb
n_p	Number of pole pairs	4
J	Rotational inertia	0.00086 $kg \cdot m^2$
P_N	Rated power	600 W
T_e	Rated torque	6 $N \cdot m$
n_N	Rated speed	1000 r/min
T_s	Sampling period	100 μs
$C_{1,2}$	DC-link capacitance	560 μF

It can be seen that both methods track the speed reference well at constant torque, and the proposed method is more stable in comparison. The results of Fast Fourier Analytical Transform (FFT) show that the Total Harmonic Distortion (THD) of phase current is 3.25% for the conventional method and 2.71% for the proposed method, which is the effect of using coherent voltage vector and zero-sequence component injection. The proposed method is able to track the d-axis current target stably with a maximum tracking error of about 0.15A, which is much lower than that of M2V-MPC. The

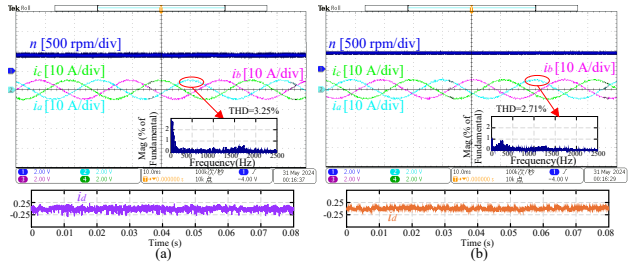

Fig. 10. Comparison of steady-state performance at rated load, 500 r/min. From above to below: speed, three-phase currents, harmonics spectrum, d-axis current. (a) M2V-MPC. (b) the proposed method.

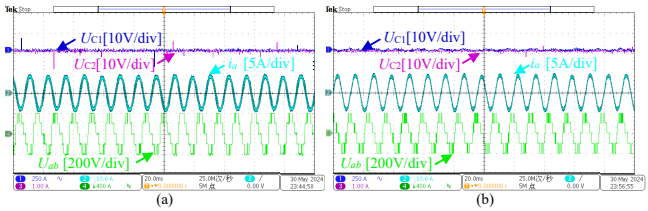

Fig. 11. Comparison of steady-state performance at rated load, 1250 r/min. From above to below: dc-link capacitor voltages, phase-a output currents, line-line voltage. (a) M2V-MPC. (b) the proposed method.

proposed method is better than MV2-MPC in terms of current quality and d-axis current ripple.

Steady-state behavior of the PMSM for the two methods is also tested at 1.25 times the rated speed (1250 r/min), and the waveforms are illustrated in Fig. 11. Although the output currents of both FCS-MPC algorithms are sinusoidal, the proposed method has a lower current distortion of 2.55%. The employment of CVVs with adjustable amplitude and moveable start point can still improve the current quality significantly during high-speed operation. It can also be seen from Fig. 11 that the neutral point voltage deviation (U_{C_1}-U_{C_2}) in the proposed method is limited to 1.18 V (peak-to-peak), while more spikes are present in M2V-MPC.

In order to quantitatively compare the steady-state performance of the motors using the two methods, the torque ripple is evaluated using the standard deviation equation.

$$\sigma_\varepsilon = \sqrt{\frac{1}{N}\sum_{n=1}^{N}(\varepsilon(n)-\varepsilon^{\text{ave}})}, \quad \varepsilon^{\text{ave}} = \frac{1}{N}\sum_{n=1}^{N}\varepsilon(n) \tag{27}$$

where N is the number of sampled data; σ_ε represents the torque standard deviation σ_{Te}, respectively; and ε^{ave} is the corresponding mean value.

The steady-state performances across the full motor speed range was experimentally investigated for both methods under rated load, with results presented in Fig. 12. The proposed method demonstrates superior performance throughout the entire speed range. Numerical comparisons indicate that the average torque ripple of the proposed method is 39.65% lower, and the average THD is 66.21% lower than that of the M2V-MPC.

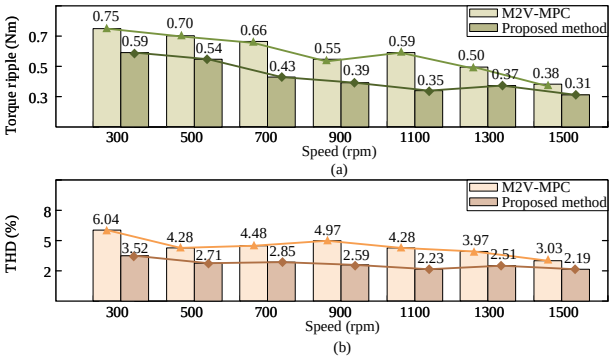

Fig. 12. Quantitative comparison of the control performance of the two methods. (a) Torque ripple. (b) THD.

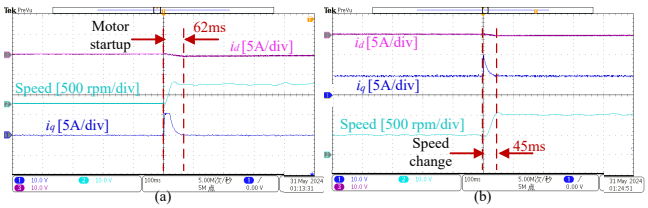

Fig. 13. Dynamic response of motor speed and dq-axis current. (a) Start from standstill to 500r/min with no load. (b) Speed change from 500 to 1000 r/min with the rated load.

B. Performance Evaluation of Transient Response

Apart from the steady-state performance comparison, the dynamic performance of the proposed method is also investigated. Fig. 13 shows the experimental results for the speed and dq-axis currents transient response. It can be observed that when the motor starts from standstill to 500 r/min with no load, the proposed method is able to realize the response within 62 ms. During the transient process, the d-axis current decreases because the motor operates within the field weakening area.

Moreover, Fig. 13(b) shows the ability of the drive to respond to a sudden change in reference speed from 500 r/min to 1000 r/min at the rated load. The rotor speed quickly reaches the rated speed in just 45ms and i_q tracks its reference well.

To highlight the tracking performance of the proposed methods during transients, Fig. 14 shows the zoomed d-axis and q-axis current transient waveforms for the two methods during the speed reversal (from forward to reverse).

It can be observed that the settling time of the proposed method is only 1.08 ms, which is 1.7 times shorter than that of M2V-MPC, and the overshoot is significantly lower. Due to

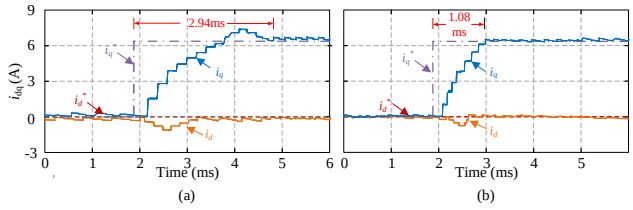

Fig. 14. dq-axis currents transient-state response during speed reversal. (a) M2V-MPC. (b) the proposed method.

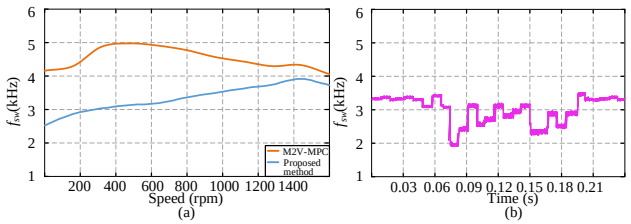

Fig. 15. Average switching frequency of the experiment at the fixed sampling frequency. (a) Comparison of f_{sw} at various speeds. (b) Responses of f_{sw} during speed reversal.

the candidate vector coherent processing, the output voltage does not change abruptly, which results in a small dq-axis current ripple, but the fast response is still maintained.

C. Investigation of Average Switching Frequency

The single carrier modulation mode and pulse train generation adopted in the proposed scheme can avoid two-level jumps and the switching loss is reduced. To highlight this advantage, the average switching frequency of the six IGBTs at the top of the 3L-NPC inverter is defined as follows

$$f_{\mathrm{sw}} = \frac{1}{6T}\sum_{k=1}^{6} N_{c_k} \tag{28}$$

where N_{c_k} is the number of state switchings of the kth IGBT during the stator period T.

For a fair comparison in the previous steady-state experiments, the average switching frequencies of the two methods were kept at approximately the same level. When the sampling frequency is controlled to be fixed, t he a verage switching frequencies of the two control schemes at different speeds are tested, and the results are shown in Fig. 15(a). It is obvious that the proposed strategy exhibits lower f_{sw} over the entire speed range, which verifies t he b enefit of li miting st ate sw itching to the two types of (0↔1) and (-1↔0). At rated speed, f_{sw} of M2V-MPC is 4.514 kHz and f_{sw} of the proposed method is 3.536 kHz. Therefore, the latter reduces the average switching frequency by 21.67% relative to M2V-MPC, although the switching frequency is not included in the cost function, and there is no need to tune the weighting factor.

Fig. 15(b) shows the switching status of the proposed method during the transient process of the previous reversal test, with f_{sw} updated every 10 ms. It can be seen that during the dynamic process, the average switching frequency temporarily fluctuates. A fter t he t ransient p rocess e nds, f_{sw} can be restored to the level before the speed reversal. The tests show that the specially designed coherent voltage vector change rapidly in response to transient changes and remain relatively stable after tracking the given value.

V. Conclusion

In this paper, a novel coherent voltage vector-based MPC method is proposed and has been experimentally applied to a PMSM system. Candidate vectors are coherently processed, and the starting point can be movable according to the optimal vector of the previous instant, thus avoiding sudden changes in the output voltage. Zero-sequence component injection is introduced to balance the neutral point potential, the amplitude of which is judged according to the sector in which the CVV with the minimum tracking error is located. Another innovative point of the proposed method is in the generation of the pulse sequence, which is not only easy to implement, but also does not involve two-step jumps. The experimental results confirmed that the proposed MPC method could achieve better output current quality in the steady-state and faster transient response in comparison with the conventional multi-vector MPC. Under the full speed range conditions, the proposed method features lower switching frequency, and the average torque ripple is reduced by 39.65%.

References

[1] M. Gu, Z. Wang, C. Wen, and Z. Zou, "Collaborative mid-point voltage regulation in low-switching-frequency mpc for three-level npc inverters fed dual three-phase pmsm drives," *IEEE Open Journal of Power Electronics*, vol. 2, pp. 673–682, 2021.

[2] C. Xiang, J. Du, X. Fu, R. Zhou, Y. Yang, and X. Zhang, "Optimization of the pulse-width-modulation strategy for three-level inverters with reduced power loss," *IEEE Transactions on Transportation Electrification*, pp. 1–1, 2024.

[3] W. Zouari, B. E. Bedsi, and A. Masmoudi, "On the design and analysis of a weighting factor free-based predictive flux control strategy for three-level npc inverter-fed im drives," *IEEE Journal of Emerging and Selected Topics in Power Electronics*, vol. 12, no. 1, pp. 923–935, 2024.

[4] J. Guo, K. Chau, W. Liu, Z. Hua, and S. Li, "Segmented-vector pulse frequency modulated three-level converter for wireless power transfer," *IEEE Transactions on Power Electronics*, pp. 1–13, 2024.

[5] Z. Zhang, X. Yang, W. Wang, K. Chen, N. C. Cheung, and J. Pan, "Enhanced sliding mode control for pmsm speed drive systems using a novel adaptive sliding mode reaching law based on exponential function," *IEEE Transactions on Industrial Electronics*, pp. 1–11, 2024.

[6] Z. Niu, Y. Zuo, H. Wang, L. Zhang, X. Zhu, and C. H. T. Lee, "Improved low-frequency disturbance rejection property for position control of pmsm using generalized extended state observer," *IEEE Journal of Emerging and Selected Topics in Power Electronics*, vol. 11, no. 5, pp. 4739–4748, 2023.

[7] W. Wang, C. Liu, H. Zhao, and Z. Song, "Improved deadbeat-direct torque and flux control for pmsm with less computation and enhanced robustness," *IEEE Transactions on Industrial Electronics*, vol. 70, no. 3, pp. 2254–2263, 2023.

[8] S. Liu, Y. Liu, B. Zhang, and C. Liu, "Full-speed region predictive current control method of symmetrical series-winding pmsm with higher dc-link utilization," *IEEE Transactions on Industrial Electronics*, vol. 71, no. 6, pp. 5541–5552, 2024.

[9] X. Yuan, S. Xie, J. Chen, S. Zhang, C. Zhang, and C. H. T. Lee, "An enhanced deadbeat predictive current control of spmsm with linear disturbance observer," *IEEE Journal of Emerging and Selected Topics in Power Electronics*, vol. 10, no. 5, pp. 6304–6316, 2022.

[10] X. Zhu, L. Xu, L. Li, W.-H. Chen, W. Fan, Z. Jin, and L. Quan, "Current decoupling model predictive control of a leakage flux controllable pm motor in virtual flux reference frame," *IEEE Transactions on Industrial Electronics*, vol. 71, no. 8, pp. 8471–8481, 2024.

[11] P. Karamanakos and T. Geyer, "Guidelines for the design of finite control set model predictive controllers," *IEEE Transactions on Power Electronics*, vol. 35, no. 7, pp. 7434–7450, 2020.

[12] H. A. Hamed, A. F. Abdou, M. S. E. Moursi, and E. E. EL-Kholy, "A modified dpc switching technique based on optimal transition route for of 3l-npc converters," *IEEE Transactions on Power Electronics*, vol. 33, no. 3, pp. 1902–1906, 2018.

[13] T. Dorfling, H. du Toit Mouton, T. Geyer, and P. Karamanakos, "Long-horizon finite-control-set model predictive control with nonrecursive sphere decoding on an fpga," *IEEE Transactions on Power Electronics*, vol. 35, no. 7, pp. 7520–7531, 2020.

[14] L. Gang, W. Dafang, W. Miaoran, Z. Cheng, and W. Mingyu, "Neutral-point voltage balancing in three-level inverters using an optimized virtual space vector pwm with reduced commutations," *IEEE Transactions on Industrial Electronics*, vol. 65, no. 9, pp. 6959–6969, 2018.

[15] Y. Yang, H. Wen, M. Fan, X. Zhang, L. He, R. Chen, M. Xie, M. Norambuena, and J. Rodriguez, "Low complexity finite-control-set mpc based on discrete space vector modulation for t-type three-phase three-level converters," *IEEE Transactions on Power Electronics*, vol. 37, no. 1, pp. 392–403, 2022.

[16] W. Alhosaini, Y. Wu, and Y. Zhao, "An enhanced model predictive control using virtual space vectors for grid-connected three-level neutral-point clamped inverters," *IEEE Transactions on Energy Conversion*, vol. 34, no. 4, pp. 1963–1972, 2019.

[17] H.-C. Moon, J.-S. Lee, and K.-B. Lee, "A robust deadbeat finite set model predictive current control based on discrete space vector modulation for a grid-connected voltage source inverter," *IEEE Transactions on Energy Conversion*, vol. 33, no. 4, pp. 1719–1728, 2018.

[18] A. Mora, R. CÃ¡rdenas-Dobson, R. P. Aguilera, A. Angulo, F. Donoso, and J. Rodriguez, "Computationally efficient cascaded optimal switching sequence mpc for grid-connected three-level npc converters," *IEEE Transactions on Power Electronics*, vol. 34, no. 12, pp. 12 464–12 475, 2019.

[19] S. G. Petkar, K. Eshwar, and V. K. Thippiripati, "A modified model predictive current control of permanent magnet synchronous motor drive," *IEEE Transactions on Industrial Electronics*, vol. 68, no. 2, pp. 1025–1034, 2021.

[20] X. Wu, Y. Zhang, F. Shen, M. Yang, T. Wu, S. Huang, and H. Cui, "Equivalent three-vector-based model predictive control with duty-cycle reconstruction for pmsm," *IEEE Transactions on Industrial Electronics*, vol. 71, no. 3, pp. 2395–2404, 2024.

[21] H. Yang, Y. Zhang, and M. Li, "Duty-cycle correction-based model predictive current control for pmsm drives fed by a three-level inverter with low switching frequency," *IEEE Transactions on Power Electronics*, vol. 38, no. 6, pp. 6841–6850, 2023.

[22] F. Donoso, A. Mora, R. CÃ¡rdenas, A. Angulo, D. SÃ¡ez, and M. Rivera, "Finite-set model-predictive control strategies for a 3l-npc inverter operating with fixed switching frequency," *IEEE Transactions on Industrial Electronics*, vol. 65, no. 5, pp. 3954–3965, 2018.

[23] W. Xie, X. Wang, F. Wang, W. Xu, R. M. Kennel, D. Gerling, and R. D. Lorenz, "Finite-control-set model predictive torque control with a deadbeat solution for pmsm drives," *IEEE Transactions on Industrial Electronics*, vol. 62, no. 9, pp. 5402–5410, 2015.

[24] X. Zhang and B. Hou, "Double vectors model predictive torque control without weighting factor based on voltage tracking error," *IEEE Transactions on Power Electronics*, vol. 33, no. 3, pp. 2368–2380, 2018.

[25] X. Li, Z. Xue, L. Zhang, and W. Hua, "A low-complexity three-vector-based model predictive torque control for spmsm," *IEEE Transactions on Power Electronics*, vol. 36, no. 11, pp. 13 002–13 012, 2021.

[26] H. Kawai, Z. Zhang, R. Kennel, and S. Doki, "Direct speed control based on finite control set model predictive control with voltage smoother," *IEEE Transactions on Industrial Electronics*, vol. 70, no. 3, pp. 2363–2372, 2023.

[27] M. Gu, Y. Yang, M. Fan, Y. Xiao, P. Liu, X. Zhang, H. Yang, and J. Rodriguez, "Finite control set model predictive torque control with reduced computation burden for pmsm based on discrete space vector modulation," *IEEE Transactions on Energy Conversion*, vol. 38, no. 1, pp. 703–712, 2023.

[28] Y. Yang, H. Wen, M. Fan, M. Xie, and R. Chen, "Fast finite-switching-state model predictive control method without weighting factors for t-type three-level three-phase inverters," *IEEE Transactions on Industrial Informatics*, vol. 15, no. 3, pp. 1298–1310, 2019.

[29] D. Zhou, L. Ding, and Y. R. Li, "Two-stage model predictive control of neutral-point-clamped inverter-fed permanent-magnet synchronous motor drives under balanced and unbalanced dc links," *IEEE Transactions on Industrial Electronics*, vol. 68, no. 5, pp. 3750–3759, 2021.

[30] M. Li, X. Jiang, C. Chen, K. Zhang, and J. Xiong, "Fault-tolerant strategy for modular multilevel converters with combined zero-sequence voltage injection," *IEEE Transactions on Power Electronics*, vol. 39, no. 7, pp. 8101–8113, 2024.

[31] X. Zhang, X. Wu, G. Tan, W. Zhang, and Q. Wang, "A dual-vector model predictive control method with minimum current thd," *IEEE Transactions on Power Electronics*, vol. 36, no. 9, pp. 9758–9762, 2021.

[32] Z. Xue, S. Niu, and X. Li, "A simplified multivector-based model predictive current control for pmsm with enhanced performance," *IEEE Transactions on Transportation Electrification*, vol. 9, no. 3, pp. 4032–4044, 2023.

[33] D. Zhou, C. Jiang, Z. Quan, and Y. R. Li, "Vector shifted model predictive power control of three-level neutral-point-clamped rectifiers," *IEEE Transactions on Industrial Electronics*, vol. 67, no. 9, pp. 7157–7166, 2020.

[34] C. Liu, X. Xing, C. Du, B. Zhang, C. Zhang, and F. Blaabjerg, "An improved model predictive control method using optimized voltage vectors for vienna rectifier with fixed switching frequency," *IEEE Transactions on Power Electronics*, vol. 38, no. 1, pp. 358–371, 2023.

[35] Y. Yang, H. Wen, R. Chen, M. Fan, X. Zhang, M. Norambuena, and J. Rodriguez, "An efficient model predictive control using virtual voltage vectors for three-phase three-level converters with constant switching frequency," *IEEE Transactions on Industrial Electronics*, vol. 69, no. 4, pp. 3998–4009, 2022.